Linking Enceladus' plume characteristics to the crevasse properties

van der Hijden, Nick J.; Giordano, Fabrizio; Oliver Scholts, Sebastian O.; Sklavenitis, Stavros; Bründl, Tara Marie; Bourgeois, Yaël R.A.; Schrijer, Ferry F.J.; Cazaux, Stéphanie M.

DOI
10.1016/j.icarus.2024.116114

Publication date
2024

Document Version
Final published version

Published in
Icarus

Icarus 417 (2024) 116114

Contents lists available at ScienceDirect

Icarus

journal homepage: www.elsevier.com/locate/icarus

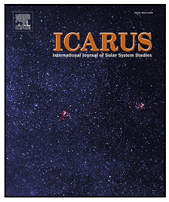

Linking Enceladus' plume characteristics to the crevasse properties

Nick J. van der Hijden [a], Fabrizio Giordano [a], Sebastian O. Oliver Scholts [a], Stavros Sklavenitis [a], Tara-Marie Bründl [a], Yaël R.A. Bourgeois [a,b], Ferry F.J. Schrijer [a], Stéphanie M. Cazaux [a,b,*]

[a] Faculty of Aerospace Engineering, Delft University of Technology, Delft, The Netherlands
[b] Leiden Observatory, Leiden University, P.O. Box 9513, NL 2300 RA Leiden, The Netherlands

ARTICLE INFO

Keywords:
Enceladus
Plumes
Crevasse
Reservoir conditions
Nucleation
Particle growth
Solid fraction
Particle size
Accretion
Sublimation

ABSTRACT

Supersonic plumes of water vapour and icy particles have been observed by the Cassini spacecraft during several flybys over Enceladus. These plumes originate from the Tiger Stripes located in the South Polar Terrain (SPT), and indicate the presence of a subsurface ocean under the icy crust which is salty and contains complex organic molecules. Other characteristics of the plumes, such as the vent temperature, mass flow rate, velocity and mass fraction of icy particles can be used to determine the conditions in the channel, linking the subsurface ocean to the icy surface. In this paper, we developed a fluid dynamics model that accounts for nucleation, particle growth, wall accretion and sublimation. The channel behaves similarly to a converging–diverging nozzle, which forms supersonic plumes due to a pressure difference between the reservoir where the subsurface ocean is located and the exosphere. The geometry of the channel and its evolution with accretion of gas and sublimation of ice are studied to reproduce the characteristics of the plumes observed by Cassini. We first performed a parameter study on the channel geometry to determine how it influences the plumes' velocity, solid fraction and exit temperature. Our results show that the size of the icy particles is primarily dependent on the length of the channel, indicating that large particles (~ 75 μm) must originate from within a kilometer below the surface, while smaller particles (~ 3 μm) can originate from only hundreds of meters below the surface. We further show that the velocity of the flow, exit temperature and nucleation depend directly on the exit-to-throat size ratio. We find that the channel geometry evolves within a few tens of hours until an equilibrium is reached, when considering the accretion of gas to the walls, or sublimation of ice from the walls. As the channel closes due to accretion, the flow becomes thinner, which in turn reduces accretion. After around 70 h, the accretion is sufficiently slowed such that the geometry does not evolve anymore. This equilibrium geometry produces higher Mach numbers and a larger particle size and solid fraction compared to the initial geometry.

1. Introduction

In 2005 the Cassini spacecraft discovered plumes of water vapour and ice particles at the south polar region of Enceladus (Porco et al., 2006). These so-called plumes are generated from surface hot spots along parallel elongated crevasses, called the "Tiger Stripes". The source of the plumes may be the vaporisation of liquid water followed by particle production via nucleation (Schmidt et al., 2008) and/or vapour sublimation from the channel walls with subsequent condensation (Kieffer et al., 2006) where grains and vapour are accelerated to the surface by pressure-driven expansion (Matson et al., 2012). Cassini observations allowed to derive several characteristics from the plumes such as their composition (Postberg et al., 2009a,b; Hansen et al., 2011; Khawaja et al., 2017), mass flow rates (Hansen et al., 2006, 2008, 2011; Burger et al., 2007; Dong et al., 2011), Mach numbers (Dong et al., 2011; Smith et al., 2010; Tian et al., 2007; Teolis et al., 2017), ice-vapour ratio (Ingersoll and Ewald, 2011; Porco et al., 2006; Kieffer et al., 2009), particle sizes (Hedman et al., 2009) and vent temperatures (Spencer et al., 2013; Tenishev et al., 2014). The intensity of the plumes, and therefore their characteristics do vary over time because of tidally driven expansion and compression of the crevasses (Porco et al., 2014) which are observed to occur on time scales in the order of days, caused by Enceladus' orbital frequency, or years due to resonances with Dione (Saur et al., 2008; Ingersoll et al., 2020).

There are several hypotheses to explain the mechanisms powering the plumes. The plumes could originate from clathrate decomposition (Kieffer et al., 2006), to explain the abundances of volatile gases, or from sublimating water ice (Nimmo et al., 2007). However, both scenarios cannot explain the identification of a sodium-rich grain population in the E-ring, with a concentration of ~ 0.5–2% in mass (Postberg

* Corresponding author at: Faculty of Aerospace Engineering, Delft University of Technology, Delft, The Netherlands.
E-mail address: s.m.cazaux@tudelft.nl (S.M. Cazaux).

https://doi.org/10.1016/j.icarus.2024.116114
Received 2 October 2023; Received in revised form 23 February 2024; Accepted 29 April 2024
Available online 6 May 2024

et al., 2009b). This amount of salt can only arise if the plumes originate from liquid water, since the ice layers are thought to be almost salt-free (Zolotov, 2007). The observed plumes' characteristics such as velocities and particle sizes have been theoretically proven to be in agreement with a reservoir near the triple point (Schmidt et al., 2008).

In Schmidt et al. (2008), a theoretical model has been developed to predict the characteristics of the plumes as a function of the channel properties, focusing on nucleation and particle production. The channels are modelled as nozzles, where variations in channel width generate the transition to supersonic speeds. This transition occurs near the throat of the channel, where nucleation is locally enhanced.

In this paper, we follow a similar approach as Schmidt et al. (2008) to determine the characteristics of the plumes depending on different channels' geometries. For this purpose, we performed a parameter study to understand how the characteristics of the plumes differ from one channel to another. In our model, the accretion of water vapour on the channel's walls is considered as well as the change in the geometry of the channel due to accretion and sublimation. We show that small channels of around 6 meters in width would become narrow (less than a meter) and reach an equilibrium within tens of hours. As the channel narrows, the expansion ratio (exit over throat ratio) increases, increasing the flow velocity, nucleation and solid fraction. However, due to fact that the channel is becoming narrower, the flow gets thinner which decreases the accretion to the walls and provides an equilibrium for the geometry.

This paper is organised as follows. In Section 2 the method used to simulate the plumes is explained, the baseline channel with the different parameters used for the study is detailed in Section 3, and in Section 4 the results for the different channels are shown. These results are discussed in Section 7, and a conclusion is drawn in Section 8.

2. Method

The fluid model is based on the conservation equations for mass, momentum and energy. The channel shape is given as input which generates the initial conditions at the inlet of the channel in terms of temperature, pressure, density and velocity. The flow is computed along the full channel length and the flow is updated in each iteration using a predictor–corrector scheme in a time-marching fashion. This is continued until a steady-state flow is reached and the convergence criteria are met. The model includes particle production from homogeneous nucleation, particle growth, sublimation of the walls and accretion onto the walls. Therefore functions describing these phenomena are included in the model that numerically determines these effects on the conservation equations. The conservation equations are used in the conservative form and are therefore suitable for shock-capturing (Anderson and Wendt, 1995). This implies that in the case that a shock is present in the channel, the discontinuous shape of the flow parameters is computed accordingly.

2.1. Governing equations

The governing equations are derived from the continuity, momentum and energy equations in their conservative form, given in Sections 2.1.1–2.1.3.

2.1.1. Continuity

The continuity equation in its conservative differential form, suitable for quasi-one-dimensional flow, accounts for mass flow into the walls, generated due to sublimation and accretion. This is realised by a sink or source term on the right-hand side of the equation, $\dot{m}_w$ [kg/(m s)] as shown in the following equation.

$$\frac{d(\rho A V)}{dz} = -\dot{m}_w \tag{1}$$

In Eq. (1), z is the vertical distance measured from the reservoir [m], ρ is the vapour density [kg/m^3], V is the velocity [m/s] and A is the cross-sectional area of the channel [m^2]. Note that we consider solid particles as part of the gas, meaning that the mass of solid particles is included in the mass of the gas. We also consider that icy particles have the same velocity as the gas. The flow is quasi-one dimensional meaning that whilst the flow properties vary in one dimension, the cross-section of the stream tubes are allowed to vary in the same direction.

2.1.2. Momentum

The momentum equation in the z-direction, for viscous flow with no body forces, is given as follows:

$$\frac{d\left(\rho V^2 A\right)}{dz} = -A\frac{dp}{dz} - \dot{m}_a V \tag{2}$$

This equation is written in conservation form for quasi-one-dimensional flow, with p denoting the pressure [N/m^2] and $\dot{m}_a$ the mass rate per unit distance of accretion onto the walls [kg/(m s)]. The second term on the right-hand side accounts for the loss of momentum due to the wall interactions and the third for friction with the walls.

2.1.3. Energy

The energy equation in its conservative differential form, suitable for quasi-one-dimensional flow, that accounts for latent heat from condensation and evaporation in the flow and energy loss to the walls, is written as:

$$\begin{aligned}\frac{d\left[\rho\left(e+\frac{V^2}{2}\right)AV + pAV\right]}{dz} &= \frac{d\left(\rho V f A\right)}{dz}L_h \\ -\dot{m}_a\left(e+\frac{V^2}{2}+\frac{p}{\rho}\right) &+ \dot{m}_s\left(e_w + \frac{p_{eq}^{s.g.}}{\rho_{eq}^{s.g.}}\right)\end{aligned} \tag{3}$$

In this equation, e [J/kg] is the specific internal energy of the flow at temperature T and e_w [J/kg] is the specific energy of the vapour sublimating from the walls at the temperature of the walls T_w; e is written as $C_v T$ with C_v = 1384.21 J/(kg K) (Peeters et al., 2002). f is the solid fraction of the mass flow, L_h is the latent heat released due to accretion of the gas, $\dot{m}_a$ is the mass flow per unit distance into the walls by accretion [kg/(m s)], $\dot{m}_s$ is the mass flow per unit distance from the walls by sublimation [kg/(m s)], and $p_{eq}^{s.g.}$ and $\rho_{eq}^{s.g.}$ are the saturated vapour pressure and density at the solid–gas equilibrium.

The first term in the left-hand side of Eq. (3) is the net flow of energy across a surface A and the second term is the work on the fluid by pressure force. The first term on the right side is the addition of heat to the flow, in the form of latent heat, the second term is the loss of energy due to accretion onto the walls and the third term is energy gain by sublimation from the walls. When mass flow is accreting on the wall e, V, p and ρ are at the level of the flow. In the case of sublimation, $e = C_v T_w$ assuming ideal gas, $V = 0$ and p and ρ are that of the saturated vapour at the solid–gas equilibrium at T_w (Nakajima and Ingersoll, 2016).

2.2. MacCormack solver

The MacCormack method solves the flow that obeys the three conservation equations with a predictor–corrector scheme based on forward and rearward differences. A time-marching approach is used in which the flow variables are updated in each iteration (Anderson and Wendt, 1995).

2.2.1. Generic form of conservation equations

The governing partial differential equations are written in a generic form. In these equations, the dependent variables are the flux vectors $(p+\rho u, \rho\left(e+V^2/2\right), etc.)$, which lead to stable solutions. This system of equations is iteratively solved. The iterative procedure starts with an initial distribution for the flow state along z in the channel, this state is then updated in each iteration, according to the conservation equations. This is done with a time-marching approach to converge

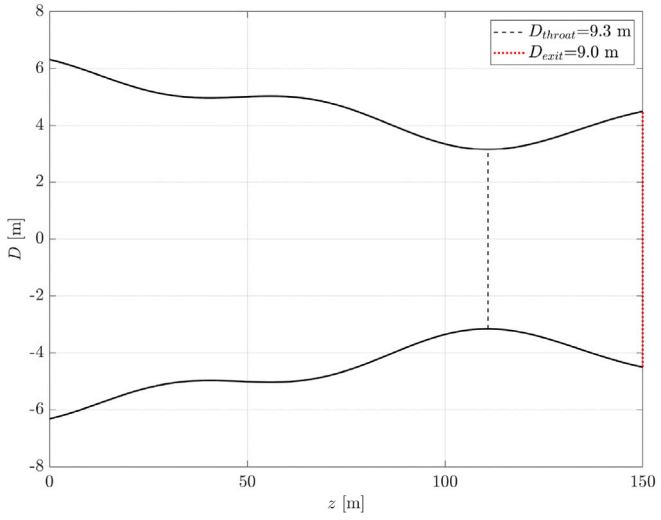

Fig. 1. Baseline channel with a D_{exit}/D_{throat} ratio of 1.4, the dashed line represents the location of the throat.

to a stable solution. The change in the solution vectors per iteration is computed with an average of the forward and rearward difference scheme (Anderson and Wendt, 1995). From the conservation equations, the entire system of governing equations is obtained:

$$\frac{\partial U}{\partial t} + \frac{\partial F}{\partial z} = J \tag{4}$$

In this system, U is the solution vector, F contains the flux terms and J is the source term. All the variables made non-dimensional are indicated with a prime symbol, resulting in the following elements of U, F and J.

$$\begin{aligned}
U_1 &= \rho' A' \\
U_2 &= \rho' A' V' \\
U_3 &= \rho' \left(\frac{e'}{\gamma - 1} + \frac{\gamma}{2} V'^2 \right) A' \\
F_1 &= \rho' A' V' \\
F_2 &= \rho' A' V'^2 + \frac{1}{\gamma} p' A' \\
F_3 &= \rho' \left(\frac{e'}{\gamma - 1} + \frac{\gamma}{2} V'^2 \right) V' A' + p' A' V' \\
J_1 &= -\dot{m}'_w \\
J_2 &= \frac{1}{\gamma} p' \frac{dA'}{dz'} - \dot{m}'_w V' \\
J_3 &= \frac{d\left(\rho' V' f A'\right)}{dz'} \cdot L'_h - \dot{m}'_a \left(\frac{e'}{\gamma - 1} + \frac{\gamma}{2} V^{2\prime} + \frac{p'}{\rho'} \right) \\
&\quad + \dot{m}'_s \left(\frac{e'_w}{\gamma - 1} + \frac{p_{eq}^{s.g.\prime}}{\rho_{eq}^{s.g.\prime}} \right)
\end{aligned} \tag{5}$$

With these elements, the conservation equations can be written as follows:

$$\frac{\partial U_n}{\partial t'} = -\frac{\partial F_n}{\partial z'} + J_n. \tag{6}$$

2.3. Initial conditions

Initial conditions $T(z = 0)$ and $\rho(z = 0)$ are computed from the total conditions in the reservoir and the initial velocity $V(z = 0)$. The numerical procedure starts at $z = 0$, where $V \neq 0$. Therefore the initial conditions are different than the total conditions in the reservoir. In the literature the triple point has $T_{res} = 273.16$ K, $\rho_{res} = 0.00485$ kg/m^3, $p_{res} = 611.2$ Pa (Porco et al., 2006; Schmidt et al., 2008).

2.4. Phase change

The vapour that is generated in the reservoir flows into the channel. Near the throat of the channel, the conditions become such that a phase change can occur, *i.e.* water vapour becomes icy particles through nucleation. This phase change is caused by a strong temperature gradient, which causes super-saturation to increase. As a result, nucleation is enhanced and a phase change is instigated. The formed particles can grow from the throat to the vent of the channel, resulting in a solid fraction being the ratio of the mass of the icy particles to the mass of the gas. In this study, we follow an identical method to Schmidt et al. (2008) to describe these processes. The gas present in the channel can accrete onto the walls, or the walls can sublimate their ices into gas phase, increasing the density of the flow. The wall interaction treatment is described in Appendix A.5.

3. Baseline channel

The baseline channel is constructed from the superposition of random harmonics, explained in Section 3.1 and taken from Schmidt et al. (2008). The parameters used to set the characteristics of the crevasses (also called channels) such as length, exit width, correlation length, expansion rate and throat location are discussed in this section.

3.1. Channel construction

The channels used in this study were constructed as described in Schmidt et al. (2008). We define the D_{min}/D_{max} ratio, exit diameter D_{exit}, channel length L and the correlation length L_0. The width of the channel as a function of z is described as follows:

$$D(z) = \sum_i A_i \sin\left(k_i z + 2\pi\xi\right) \tag{7}$$

In this equation, ξ is a uniformly distributed random number between 0 and 1. The amplitudes of the modes A_i and the wave numbers k_i are computed with the following expressions:

$$A_i = \frac{a}{\sqrt{1 + \left(k_i L_0\right)^2}} \tag{8}$$

$$k_i = \frac{1}{2}\left(\frac{2\pi}{L}\right) i < k_c = \left(\frac{2\pi}{L_0}\right) \tag{9}$$

The subscript i runs from 1 to n while $k_i < k_c$. With the parameters chosen as in Table 1, we find a series of fitting crevasses, among which one is selected as the baseline. The chosen profile is shown in Fig. 1. Subsequently, the parameters in Table 1 are varied to generate other profiles to compare with the baseline (see Section 4).

3.2. Channel main parameters

The channel geometry has been described in the previous section and depends on parameters such as length, width (exit and throat), as well as throat location. For the length, the estimated crustal thickness of Enceladus ranges from 70 km thick to a minimum of 1.5 km thick (Čadek et al., 2016; Lucchetti et al., 2017; Nimmo et al., 2007). These regions of minimum thickness are located at the South Polar Terrain (SPT) of Enceladus, where the plumes are located. It is estimated that approximately 90% of the cracks' height is filled up with water due to the difference in densities of water and ice (Nakajima and Ingersoll, 2016). Therefore, the channel length baseline is set at 150 m, based on estimates for the crustal thickness as determined by Schmidt et al. (2008). The exit width is set at 9 m for the baseline channel as in Schmidt et al. (2008), and the throat location at 111 m. The correlation length for a channel length of 150 m is chosen equal to 60 m.

In Table 1 the properties of the baseline channel are reported. The geometry of the channel is illustrated in Fig. 1.

Table 1
Summary of the baseline multi-phase channel properties.

L	D_{exit}	D_{throat}	L_0	z_{throat}	Reservoir
150 m	9 m	6.3 m	60 m	111 m	Triple point

Table 2
Summary of the parameter study, listing channel number (from 1 to 6), name, and parameters modified with respect to the baseline model.

Test case	Changes compared to baseline
1 Isentropic	Baseline with isentropic flow
2 multi-phase	Baseline multi-phase model (MPM)
3 Throat	MPM, throat location upstream
4 $\uparrow D_{exit}/D_{throat}$	MPM, smaller throat size
5 Length	MPM, channel length doubled
6 Wall interactions	MPM, evolving geometry

4. Results

In this section, the results of the different channel geometries are presented. First, the results determined by the isentropic model are presented in Section 4.1. The results of the multi-phase model are shown in Section 4.2to Section 4.5, changing the throat location and the throat diameter. In Section 4.6 wall interactions are included in the model.

A parameter study is performed on each of the variable parameters to determine what the dependencies are. The different test cases are presented in Table 2, where the second column reports the parameter which is changed with respect to the baseline (Fig. 1).

4.1. Case 1: Baseline, isentropic model

The results from the isentropic model show the characteristics of the flow due to the pressure difference between inlet and outlet, generated from the baseline reservoir at triple point conditions.

In Fig. 2, the Mach number M, temperature T, density ρ and super-saturation S of the flow are represented with solid lines. The flow reaches $M = 1$ at the throat, whose position is indicated with a dashed line, and expands further to $M = 1.76$ at the exit. As the velocity increases along the z-axis, the temperature of the flow decreases, *i.e.* internal energy ($C_v T$) is converted to kinetic energy ($1/2V^2$). The pressure decreases isentropically, to match the back pressure and, as a result, the density of the gas also decreases. The expanding gas, starting at 270 K near the reservoir, reaches a temperature of $T = 180$ K at the vent. At these low temperatures, the super-saturation degree becomes larger than one, which suggests a phase change and therefore particle production. This is afterwards added to the model and presented in Section 4.2.

4.2. Case 2: Baseline, multi-phase model

The multi-phase model considers nucleation along with particle growth and the corresponding solid fraction, stated in Appendix A.1, Appendix A.2 and Appendix A.3, respectively. The flow is computed for the baseline channel illustrated in Fig. 1, starting from triple point conditions in the reservoir.

In Fig. 3, the solid lines represent the Mach number M, temperature T, density ρ and super-saturation S of the baseline and the dashed lines those of the isentropic model. The flow is very similar to that of the isentropic model up until the throat. At this location, the super-saturation level S is lower than in the isentropic model because of phase change, which transforms gas phase molecules into solid particles. Because of the latent heat released due to this phase change, the temperature of the flow increases after the throat. The higher temperature implies a lower Mach number.

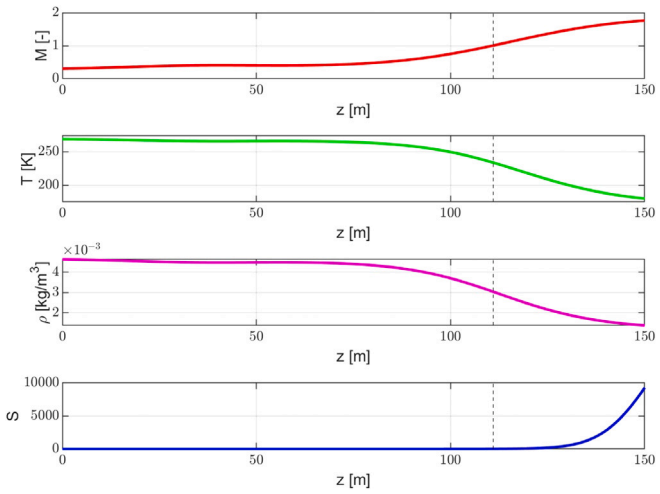

Fig. 2. M, T, ρ and S profiles of the plume, the dashed line represents the location of the throat.

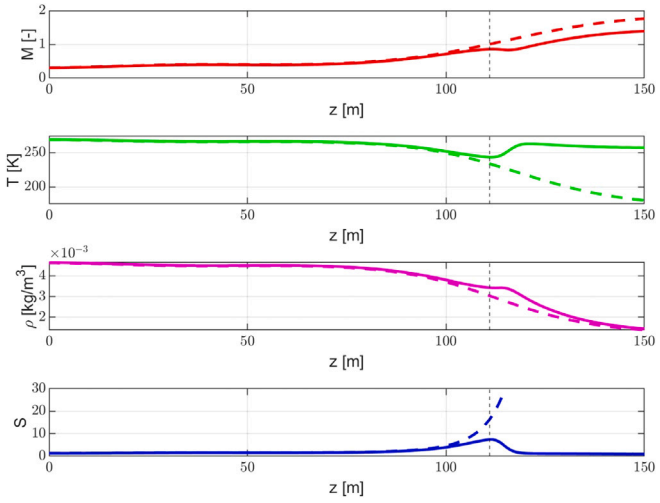

Fig. 3. M, T, ρ and S profiles of the baseline channel computed with the multi-phase model (solid lines) and the isentropic model (dashed lines). The vertical dashed line represents the location of the throat of the channel.

As a result of the increase in S, the nucleation rate γ_{nuc} increases, as illustrated in the upper panel of Fig. 4, and icy particles are formed. Due to nucleation and particle growth, the solid fraction f increases. Fig. 4 also highlights the proportionality of growth rate dR/dz to the difference between the gas density and the equilibrium density $\rho - \rho_{eq}$. Therefore, the growth rate dR/dz, being positive, indicates that the particles grow along the channel, with a decreased rate after the throat.

In the channel, there is a constant rate of mass flow, in accordance with the conservation of mass and the principle of choked flow. The flow velocity V is dependent on both the cross-section of the channel A and the density of the flow ρ, as suggested by the expression of the mass flow rate:

$$\dot{m}_{flow} = \rho A V \tag{10}$$

Therefore, an increase of ρ causes the flow to slow down, since mass flow rate $\dot{m}_{flow}$ is constant. Due to the local increase in density near the throat, the Mach number at the throat is slightly lower than 1 (Fig. 3). After the throat, the flow reaches the sonic speed due to the release of latent heat which increases the kinetic energy. Therefore the transition to supersonic speeds does not occur at the throat, but slightly downstream from it.

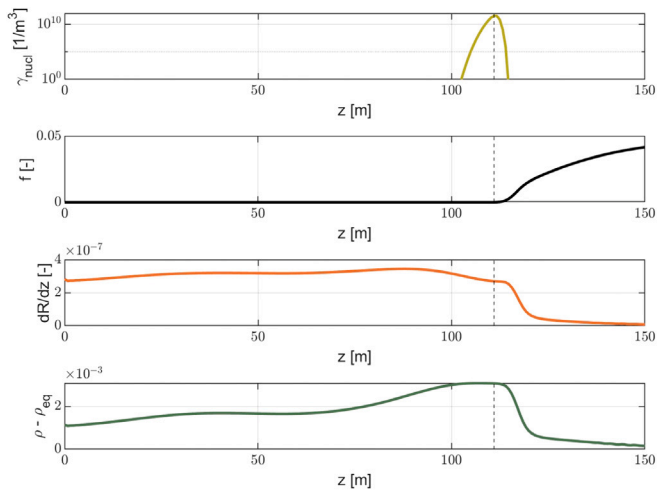

Fig. 4. γ_{nuc}, f, dR/dz and $\rho - \rho_{eq}$ profiles of the baseline channel, computed with the multi-phase model. The dashed line represents the location of the throat.

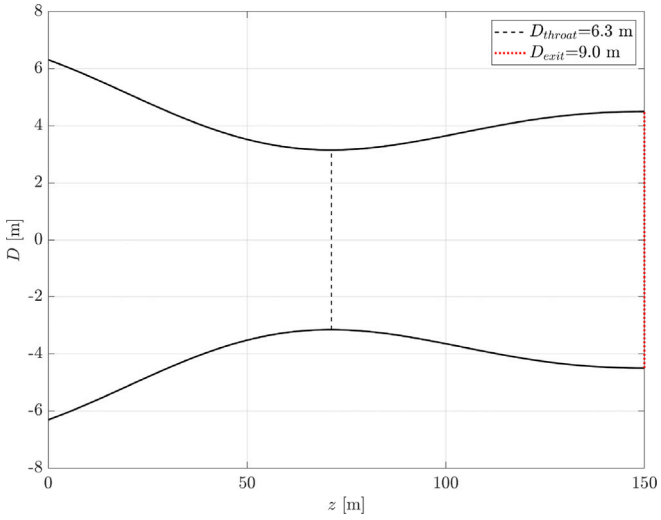

Fig. 5. Channel with a D_{exit}/D_{throat} ratio of 1.4 and the throat located at $z = 71$ m, indicated by the dashed line.

The particle growth results in particles with a mean radius of $R = 2.8$ μm and the solid fraction reaches 4.1% at the end of the channel (Fig. 4).

4.3. Case 3: Throat location, multi-phase model

In this section, the throat location is moved upstream to $z = 71$ m to determine the effect on the characteristics of the flow. The channel geometry is presented in Fig. 5.

In Fig. 6, the Mach number, temperature, density and super-saturation of the multi-phase case with a different throat location are presented in solid lines, and the same multi-phase baseline model parameters in dashed lines. The peak in super-saturation S occurs at the throat, in this case located upstream compared to the baseline. The expansion ratio is the same for both channels, resulting in similar vent conditions for the Mach number, temperature, density and solid fraction.

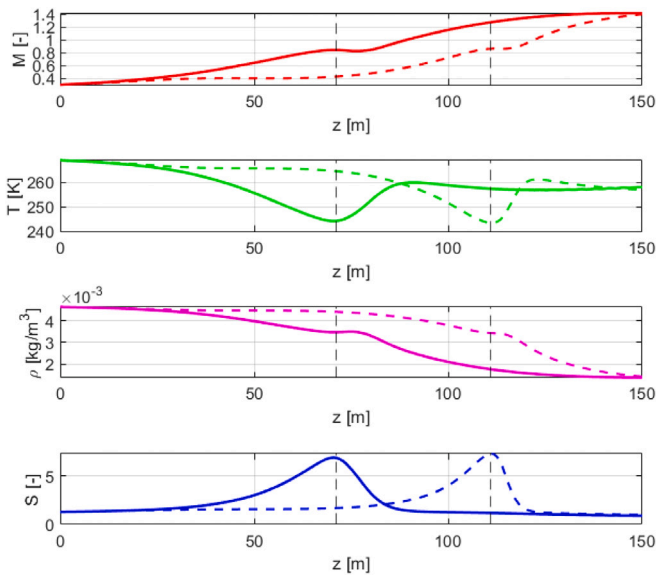

Fig. 6. M, T, ρ and S profiles of the baseline channel. The solid lines represent the results for the channel with the new throat location, the dashed lines are the results of the baseline channel, and the vertical dashed lines represent the locations of the throats.

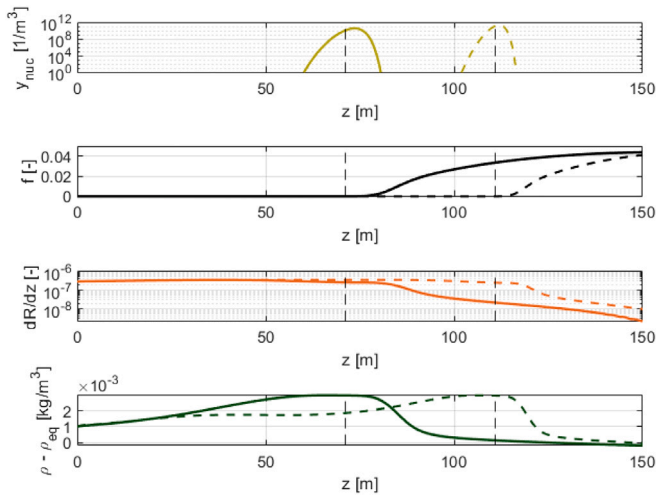

Fig. 7. γ_{nuc}, f, dR/dz and $\rho - \rho_{eq}$ profiles. The solid lines are the results of the channel with the new throat location, the dashed lines are the results of the baseline channel, and the vertical dashed lines represent the locations of the throats.

In Fig. 7, the solid lines represent the nucleation rate, solid fraction, growth rate and difference between flow density and equilibrium density of the multi-phase model with different throat location. The multi-phase baseline model is represented by dashed lines. The peak in γ_{nuc} occurs more upstream, therefore the formed particles can grow over a longer distance, resulting in larger final particle sizes. Specifically, the particles at the vent are larger in size compared to the baseline, reaching a mean size of 4.5 μm. However, the peak in γ_{nuc} is lower than in the multi-phase baseline model, resulting in a smaller amount of icy particles. Since f depends both on γ_{nuc} and the growth rate dR/dz, it is only marginally increased from 4.1% to 4.4% at the vent when the two controlling parameters are integrated over the distance z (Appendix A.3).

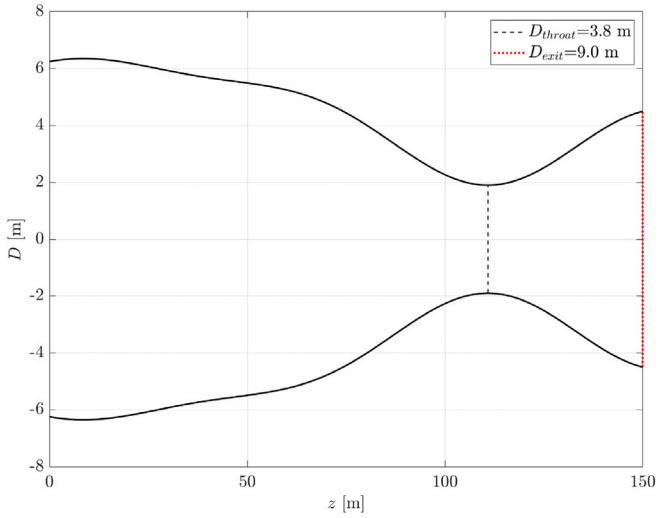

Fig. 8. Channel with a D_{exit}/D_{throat} ratio of 2.4 and the throat located to $z = 111$ m, indicated by the dashed line.

4.4. Case 4: Smaller throat size, multi-phase model

In this section, the D_{exit}/D_{throat} ratio is changed from 1.4 to 2.4 to visualise the effect of a faster expansion on the flow parameters (see Fig. 8).

In Fig. 9, the Mach number, temperature, density and super-saturation of the smaller throat case are represented with solid lines, while the multi-phase baseline model with dashed lines. For the smaller throat case, the geometry contraction rate near the throat is higher, causing the flow to accelerate faster. The flow travels faster, resulting in fewer collisions between vapour molecules in the section just before the throat. As a result, there is less heat generated by accretion, which causes the temperature T to be lower and the super-saturation S to be higher in the throat.

At the vent, we observe that the exit Mach number increases to 1.75 and the temperature to 249 K compared to the multi-phase baseline model, which can be explained by a larger D_{exit}/D_{throat} ratio (Anderson and Wendt, 1995).

In Fig. 10, the nucleation rate, solid fraction, growth rate and difference between flow density and equilibrium density of the multi-phase model with smaller throat are presented in solid lines, while the multi-phase baseline model parameters are presented in dashed lines. The temperature change in the smaller throat case is +1.5 K and the super-saturation has increased by 1.25. As a result, γ_{nuc} in the throat is 18 times larger in the smaller throat case than in the baseline. This implies that more particles are produced near the throat, resulting in a larger solid fraction $f = 6.9\%$. This causes the transition to supersonic speeds to occur relatively more upstream and the temperature to increase faster just after the throat, since in that region more energy is added to the flow as latent heat. The growth rate dR/dz is smaller compared to the baseline case, resulting in a smaller mean particle size $R = 1.5$ μm.

4.5. Case 5: Increased channel length, multi-phase model

We computed the flow characteristics, as for the previous cases, for a channel with a length of 300 m. The geometry of the baseline channel is doubled with respect to z, with the throat and exit sizes staying similar to the baseline. The results for the flow parameters are almost identical to the ones of the baseline channel since the shape of the channel is the same. However, the particles produced at the throat can grow over a longer distance for a longer channel, which increases the mean particle radius to $R = 5.4$ μm. The increased channel length therefore produces particles with larger sizes.

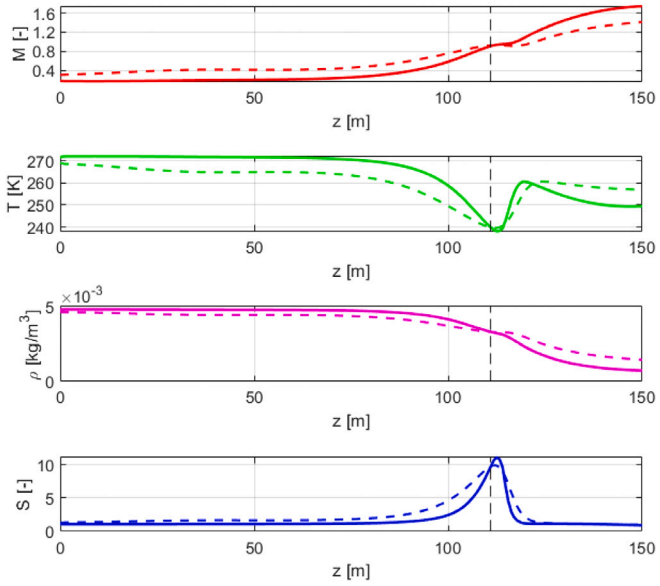

Fig. 9. M, T, ρ and S profiles of the channel with a smaller throat (solid lines), compared to the baseline channel (dashed lines). The vertical dashed line represents the throat of the channel.

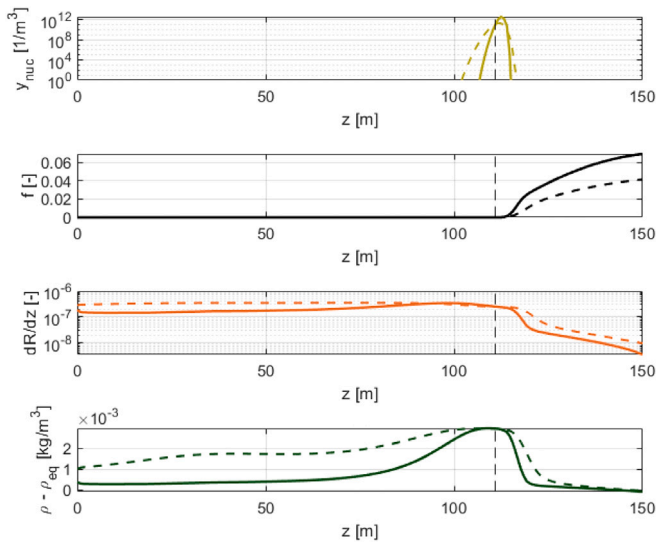

Fig. 10. γ_{nuc}, f, dR/dz and $\rho - \rho_{eq}$ profiles of the channel with a smaller throat (solid lines) and the baseline channel (dashed lines). The vertical dashed line represents the location of the throat.

4.6. Case 6: Wall interactions, multi-phase model

In this section, the wall interactions are considered in the multi-phase model. Sublimation of the ice from the walls and accretion of the gas from the flow are both changing the geometry of the channel. The description of these two processes in our model is detailed in Appendix A.5. With the conditions present in the channel, the accretion to the walls dominates over the sublimation from the walls, implying that the channel cross-section decreases with time. We estimated accretion and sublimation along the channel and found that accretion is dominating by at least one order of magnitude. The flow characteristics at the beginning of the simulations are identical to those of Case 2. For each time interval, the geometry of the channel varies due to accretion, which also implies that the flow characteristics are changing. We defined time steps of one hour to update the geometry of the

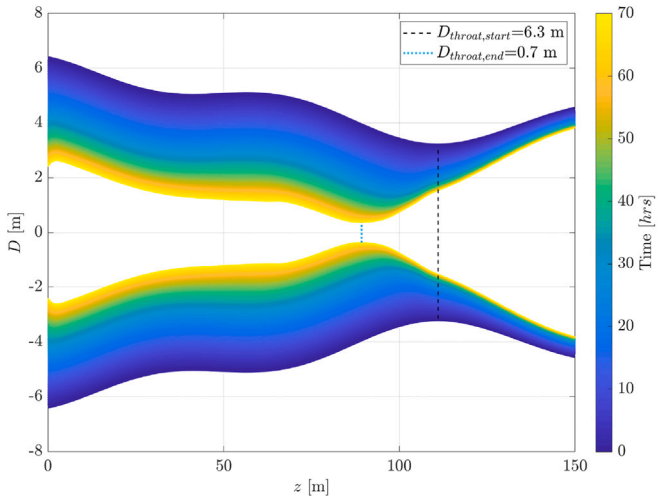

Fig. 11. Geometry of the channel with time. The different lines show how the baseline channel geometry evolves due to accretion, with each line's colour indicating the duration since accretion initiation. (For interpretation of the references to colour in this figure legend, the reader is referred to the web version of this article.)

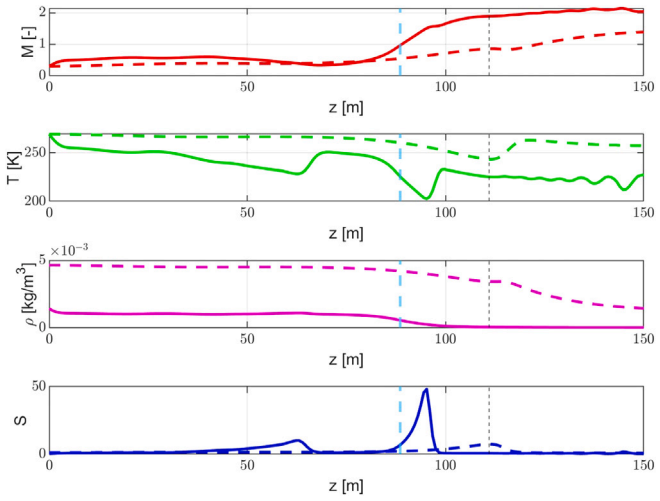

Fig. 12. M, T, ρ and S profiles of the baseline channel with accretion at the end of our 100-hour simulations (solid lines), compared to the initial baseline channel (dashed lines). The vertical dashed lines indicate the location of the throat at the end of our simulations (cyan) and at the beginning with the baseline channel (black).

Table 3
Numerical results of the different cases.

Isentropic, multi-phase and wall interactions models.						
Case	M_{exit}	V	f	T_{exit}	R	$\dot{m}$
	–	m/s	%	K	μm	kg/s
1 Isentropic	1.8	587	–	180	–	1464
2 Multi-phase	1.41	562	4.1	257	2.8	1460
3 Throat	1.41	558	4.4	258	4.5	1435
4 ↑ D_{exit}/D_{throat}	1.75	684	6.9	249	1.5	872
5 Length	1.41	550	4.3	257	5.4	1440
6 Wall interactions	2.1	760	10	220	max 7.5	<40
Cassini observations						
		350–950	7–20	170–210	0.1–75	100-1000

channel due to accretion. The MacCormack method is used to find the flow solutions after each time step, which means after each update of the channel geometry. These flow solutions are then used to determine the accretion and sublimation values from which the geometry for the next time step is calculated. The process is repeated until negligible changes in the channel geometry are observed. The evolution of the channel geometry with time is presented in Fig. 11 for a total simulated period of 70 h. Compared to the initial geometry, the channel width decreases and the throat moves upstream and becomes very narrow (0.70 m). The flow characteristics at the end of a 100-hour simulation are represented in Figs. 12 and 13. Our simulations show that as the channel narrows, the flow density and the mass flow rate decrease, leading to a reduced accretion rate over time. This implies that after a long period, accretion becomes inefficient and the channel geometry does not change significantly. Moreover, while the throat becomes narrower, the exit cross section changes marginally, which increases the expansion ratio (D_{max}/D_{min}) with time. Therefore, the evolution of the channel results in a narrow throat, a large expansion ratio, elevated vent velocity and solid fraction. Finally, Fig. 11 shows that a second throat may be forming downstream, around z=50–60 m. Flow velocity and temperature are also affected, as visible from Fig. 12. The narrowing of the passage leads to increased Mach numbers and a decrease in temperature.

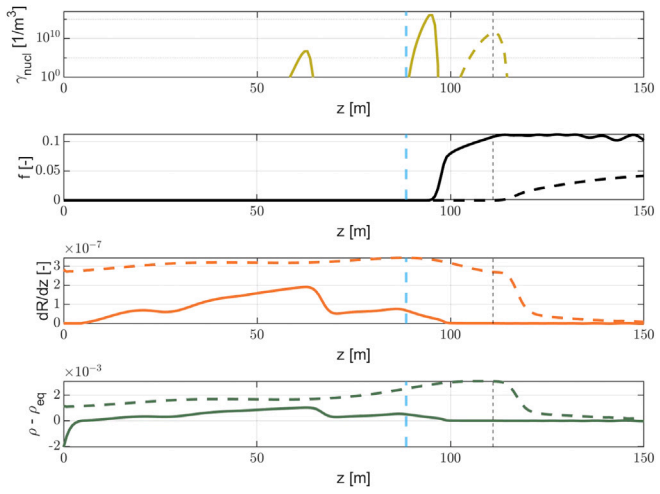

Fig. 13. γ_{nuc}, f, dR/dz and $\rho - \rho_{eq}$ profiles of the baseline channel with accretion at the end of our a 100-hour simulations (solid lines), compared to the initial baseline channel (dashed lines). The vertical dashed lines indicate the location of the throat at the end of our simulations (cyan) and at the beginning with the baseline channel (black).

5. Linking plume characteristics and channel properties

Summarising the results of the parameter study, we can determine some links between the plume characteristics and the channel geometry. Increasing the ratio of the exit diameter over throat diameter D_{exit}/D_{throat} will increase the Mach number M and velocity V (Anderson and Wendt, 1995). This lowers the temperature T and increases the super-saturation S in the throat, the nucleation rate γ_{nuc} and the formation of icy particles. Since particles form, the solid fraction f also increases with D_{exit}/D_{throat}.

The growth rate dR/dz decreases with increasing expansion ratio, caused by a rapid decrease in density ρ due to the expansion. As a result, the particle size decreases with the expansion ratio. However, we find that the length of the channel and the location of the throat have an important effect on the particle size R because, for a longer channel, particles spend a longer time in the flow, which allows them to grow to larger sizes.

6. Constraining Enceladus' crevasse properties from Cassini data

Since the plumes' parameters can be linked to the channel geometry, in this section we will report those parameters determined by Cassini's measurements and the constraints they provide on the geometry of the channel. The surface temperature T of the Tiger Stripes' fissures is measured by the CIRS to be at least 170 K (Spencer et al., 2009). The hot spots along the Tiger Stripes are measured to have temperatures of $T = 210$ K, obtained from UVIS and VIMS data (Tenishev et al., 2014). The large spread of the particle sizes could be explained by a set of channels whose throats are at different depths. In the current model, we consider that nucleation occurs at the throat of the channel. However, as boiling occurs in the reservoir (Ingersoll and Nakajima, 2016), bubbles from the liquid can burst and form a mix of vapour and tiny droplets. These particles, originating from the reservoir, can grow along a longer distance before reaching the surface, so significantly larger particles near the vent will be obtained. Such a process is not considered in the present study and would result in larger particles.

The solid fraction f is determined with UVIS and ISS data, which give the mass ratio of the water ice grains and water vapour at 7–30 km and 15 km altitude, respectively. By considering different particle size distributions, using the effective particle size ranging from 0.5–2 μm and the breadth of the particle size distribution ranging from 0.1–0.25 μm, a solid fraction of 0.1–0.2 has been determined (Kieffer et al., 2009) and of 0.07 when considering irregular aggregates (Gao et al., 2016). However, only small grains can be present and exclusively ascending at such altitudes (Kieffer et al., 2009), which implies that the obtained solid fraction f by Kieffer et al. (2009) and Gao et al. (2016) can in reality be higher or lower due to the dynamics of larger particles.

The plume velocity is estimated between 350–950 m/s by fitting the UVIS and INMS data (Tian et al., 2007; Dong et al., 2011; Smith et al., 2010). Teolis et al. (2017) estimate higher velocities to fit the peak of the CO_2 abundances in the plume, where 12% of the plume is estimated to have a Mach number of 16. The mass flow is estimated between 100–1000 kg/s from UVIS stellar and solar occultations. These estimates vary with the flyby number, $E14$, $E17$, $E18$ (Teolis et al., 2017) and $E4$ and $E5$ (Dong et al., 2011; Smith et al., 2010) and depending on whether stellar or solar occultations are used (Jurac and Richardson, 2005; Burger et al., 2007).

A channel that reproduces these plume characteristics observed by Cassini has a length of 150–1000 m to generate particles of sizes ranging from 0.1–75 μm, a large expansion ratio D_{exit}/D_{throat} close to 4 and a reservoir temperature that is probably close to 273.16 K. This strongly expanding section near the throat is needed to reach sufficiently high velocities (up to 950 m/s) near the surface that reduces the exit temperature below 210 K and generates a solid fraction in the range of 0.07–0.2. Assuming a vent 9 m wide and 200 m long, as estimated by Schmidt et al. (2008), a total mass flow rate between 800 and 1500 kg/s is estimated.

When considering wall interaction, we showed that the channel shape changes over time due to accretion and that the changes can occur on short timescales. As the channel becomes narrower, the expansion ratio becomes larger, which in turn accelerates the flow. Such a channel, which we consider reaching an equilibrium, is well reproducing the vent temperature, velocity, as well as the solid fraction and larger grain sizes measured by Cassini. In this case, the mass flow rate decreases with the channel width, reaching values below 40 kg/s with the venting area assumed above.

7. Discussion

Our parameter study has shown that the characteristics of the plumes can be linked to the geometry of the channel. However, the present model does not take into account several aspects of the plumes' dynamics as well as the channel characteristics that are discussed here.

In the model, the velocity of the grains and vapour is considered to be equal, which is not in agreement with Schmidt et al. (2008). The grains and gas are coupled if the gas density is high enough, but when the density decreases they decouple. The majority of the grains travel at 2/3 of the velocity of the gas (Schmidt et al., 2008), which could result in icy grains in slightly larger sizes and larger solid fractions. In the present work, we consider nucleation of pure water ice clusters to obtain the icy grain sizes. However, salty grains, supposedly formed as liquid droplets freeze, could also grow through accretion, and this growth rate should be larger than the nucleation rate (since the particles are larger and have larger cross sections). The salty particles should then have larger sizes than pure water ice clusters.

The venting area is assumed to be rectangular, with a venting length along the Tiger Stripes and a width orthogonal to this length. Despite the Tiger Stripes being 500 km long, the intensity of the plume along these Tiger Stripes is not constant and the majority of the plume mass flow originates from hot spots along the Tiger Stripes (Burger et al., 2007; Tenishev et al., 2014). This makes the venting length much smaller than the entire area of the Tiger Stripes. A venting area of 200 m long and 9 m wide is estimated in the work of Schmidt et al. (2008) and 3750 m^2 in the work of Nakajima and Ingersoll (2016). Using a venting area of 9 m width and 200 m long, we estimated mass flow rates of the different channels reported in Table 3. The mass flow rates obtained range between 800 to 1500 kg/s when wall interactions are not considered. These mass flow rate estimates are in agreement with the ranges determined by Cassini observations.

In the present study, we computed the interaction of the flow with the walls, and how such interaction would change the geometry of the channel. Our results show that accretion is dominant in the channel and that the channel will become narrower with time. However, the plumes' intensities are measured to vary over Enceladus' orbital period, meaning that the crevasses do open again (Ingersoll et al., 2020). The mechanism for opening the cracks is the diurnal tides experienced by Enceladus (Spencer et al., 2018). While we suggest that channels can become thin and reach an equilibrium on short timescales due to accretion, we do not consider other effects that would re-open these channels in the present study.

8. Conclusion

In this study we linked plume characteristics to a set of crevasse properties, being the channel's length, width, throat size and throat location. We presented a purely isentropic model, a multi-phase model and a model that includes wall interactions. The multi-phase model considers nucleation and particle growth, resulting in a phase change of the saturated vapour. The model with wall interactions considers accretion onto and sublimation from the walls. The plume characteristics computed from Cassini observations can be reproduced by a plume model containing nucleation, particle growth and wall interactions.

The links between the plume characteristics and the crevasse properties that were determined from this study are summarised below.

- The mean particle size is proportional to the length of the channel (*e.g.*, the particles have more time to grow over a longer channel and vice versa).
- The velocity of the flow and the exit temperature depends directly on the exit to throat size ratio. Larger ratios enable a larger expansion, increasing the flow velocity and decreasing the flow temperature.
- The icy grain nucleation depends directly on the expansion, set by the ratio of the exit to throat area.
- The wall interactions alter the channel's geometry due to accretion. An equilibrium geometry can be reached within a few tens of hours, which increases the flow velocity and solid fraction.

Our parameter study provided qualitative estimates of the channel geometry to reproduce Cassini's measurements of the plumes. To form large grains of 75 μm, large channels of the order of the kilometer are needed, while the small grains observed can be explained by channels of hundreds of meters. The high velocities observed require a high expansion ratio. Our results show that the channel geometry evolves due to gas accretion onto the walls, which makes the channel narrower until an equilibrium geometry is reached. This geometry allows for higher velocity flows and a larger solid fraction. Whether this geometry is unique on Enceladus and how it depends on the initial channel geometry will be investigated in a follow-up paper.

CRediT authorship contribution statement

Nick J. van der Hijden: Conceptualization, Data curation, Formal analysis, Investigation, Methodology, Resources, Software, Validation, Visualization, Writing – original draft, Writing – review & editing. **Fabrizio Giordano:** Conceptualization, Data curation, Formal analysis, Investigation, Methodology, Validation, Visualization, Writing – original draft, Writing – review & editing. **Sebastian O. Oliver Scholts:** Data curation, Investigation, Validation, Writing – original draft, Writing – review & editing. **Stavros Sklavenitis:** Conceptualization, Data curation, Formal analysis, Investigation, Methodology, Validation, Visualization, Writing – original draft, Writing – review & editing. **Tara-Marie Bründl:** Formal analysis, Methodology, Writing – original draft, Writing – review & editing. **Yaël R.A. Bourgeois:** Conceptualization, Investigation, Methodology, Supervision, Validation, Writing – original draft. **Ferry F.J. Schrijer:** Conceptualization, Methodology, Supervision, Visualization, Writing – original draft, Writing – review & editing. **Stéphanie M. Cazaux:** Conceptualization, Funding acquisition, Supervision, Writing – original draft, Writing – review & editing.

Declaration of competing interest

The authors declare that they have no known competing financial interests or personal relationships that could have appeared to influence the work reported in this paper.

Data availability

Data will be made available on request.

Acknowledgements

We would like to thank Prof. Jürgen Schmidt and Prof. Nikolai Brilliantov for their help and for sharing their data so that we could validate this model, as well as their useful comments and suggestions.

Appendix. Phase change

A.1. Nucleation

To compute the nucleation rates, we use an empirical function which was established for the homogeneous nucleation of D_2O and H_2O (Wölk et al., 2002). The empirical relation has been tested with experimental data (Viisanen et al., 1993) and later on a correction factor has been applied to this formula to account for a re-calibration of the pressure in the experiments (Wölk and Strey, 2001).

The empirical nucleation function for H_2O is valid for the range of nucleation rates $1 < \gamma_{nuc}[\mathrm{cm^{-3}s^{-1}}] < 10^{20}$, temperatures between $200 < \mathrm{K} < 310$ and super-saturation levels between $5 < S < 200$.

This empirical function is based on the classical nucleation theory. The Becker–Döring nucleation rate $\gamma_{nuc,BD}$ is given by Wölk et al. (2002):

$$\gamma_{nuc,\mathrm{BD}} = \sqrt{\frac{2\sigma}{\pi m}}\, v_m \left(\frac{p_v}{kT}\right)^2 e^{\left(\frac{-16\pi v_m^2\sigma^3}{3(kT)^3(\ln S)^2}\right)} \tag{11}$$

In Eq. (11), p_e and p_v are the equilibrium and the actual vapour pressures, $S = p_v/p_e$ is the super-saturation, T is the temperature, k is the Boltzmann constant and m, v_m and σ are the mass of the water molecule, the molecular volume and the surface tension of the critical cluster, respectively. Lastly, a correction factor is added to the nucleation rate (Wölk and Strey, 2001):

$$\gamma_{nuc,\mathrm{H_2O}} = \gamma_{nuc,\mathrm{BD}} \exp\left(-27.56 + \frac{6.5\cdot 10^3}{T}\right) \tag{12}$$

The nucleation rate γ_{nuc} equation is dominantly dependent on the super-saturation level S of the flow and the temperature T. S is calculated with the following expression:

$$S = \frac{\rho_{\mathrm{gas}}}{\rho_{\mathrm{eq}}^{(l.g.)}\left(T_{\mathrm{gas}}\right)} \tag{13}$$

In this equation, $\rho_{\mathrm{eq}}^{(l.g.)}$ is the saturated vapour density for the liquid–gas equilibrium, at T_{gas}. The liquid–gas equilibrium is used instead of the solid–gas equilibrium because of the small size of the water nuclei, following the argumentation in Schmidt et al. (2008).

The following expression is used to derive the equilibrium pressure ($p_{\mathrm{eq}}^{(\mathrm{l.g.})}$):

$$\begin{aligned} p_{\mathrm{eq}}^{(\mathrm{l.g.})}\left(T_{\mathrm{gas}}\right) = 610.8\exp[\,&-5.1421\ln\left(T_{\mathrm{gas}}/273.15\right)\\ &-6828.77\left(1/T_{\mathrm{gas}} - 1/273.15\right)\,] \end{aligned} \tag{14}$$

The equilibrium density is then derived from this values of $p_{\mathrm{eq}}^{(\mathrm{l.g.})}$ using the equation of state.

A.2. Particle growth

Nucleation is the first step in a phase transition, which forms particles that are larger than the critical radius r^* (Wölk and Strey, 2001). Subsequently, the particles start to grow caused by accretion of the surrounding gas. The growth rate of the grains is computed with the following equation, based on the calculation of the collision rate of water molecules with icy grains (Schmidt et al., 2008):

$$\frac{dR}{dz} = \frac{\beta}{\sqrt{2\pi\gamma}\rho_{\mathrm{grain}}}\left[\rho_{\mathrm{gas}}\,(z) - \rho_{\mathrm{eq}}^{(s.g.)}\left(T_{\mathrm{gas}}(z)\right)\right]\frac{c_s(z)}{u_{\mathrm{gas}}(z)} \tag{15}$$

In this equation, β is the fraction of adsorbed molecules from those which hit the grain, and is set to 0.2, $c_s(z)$ is the local speed of sound, equal to $\sqrt{\gamma RT}$ with γ and R being respectively the ratio of specific heat and the specific gas constant for water vapour and u_{gas} is the velocity of the gas [m/s]. The term between brackets accounts for the evaporation of molecules from the surface of the grains, which decreases the radius of the grains, which occurs when the density of the vapour ρ_{gas} is smaller than that of the saturated vapour $\rho_{eq}^{(s.g.)}$ at temperature T_{gas}. Here it is assumed that the grains have the same temperature as the gas and are crystalline, since they are formed above 160 K.

The growth rate depends on the difference between ρ_{gas} and $\rho_{eq}^{(s.g.)}$, and therefore the grains stop growing when ρ_{gas} equals $\rho_{eq}^{(s.g.)}$. The saturated vapour density $\rho_{eq}^{(s.g.)}$ is calculated as follows (Marti and Mauersberger, 1993; Peeters et al., 2002; Schmidt et al., 2008):

$$p_{\mathrm{eq}}^{(s.g.)}\left(T_{\mathrm{gas}}\right) = e^{\left[\left(-2663.5/T_{\mathrm{gas}}+12.537\right)\ln(10)\right]} \tag{16}$$

A.3. Solid fraction

The solid fraction $f(z)$ is defined as the mass flow of icy grains divided by the total mass flow. Schmidt et al. (2008) provides the following expression for the derivative of the solid fraction:

$$\begin{aligned} f'(z) = \frac{4\pi\rho_{\mathrm{grain}}}{Q}\int_0^z \gamma_{\mathrm{nuc}}\,(z_0)\left[R(z) - R(z_0)\right]^2\\ R'(z)A(z_0)\Theta_H\,R(z) - R(z_0)dz_0 \end{aligned} \tag{17}$$

In this equation ρ_{grain} is the density of the icy grains, set at 920 $\mathrm{kg/m^3}$, Q is the total mass flow, γ_{nuc} is the nucleation rate, R is the maximal

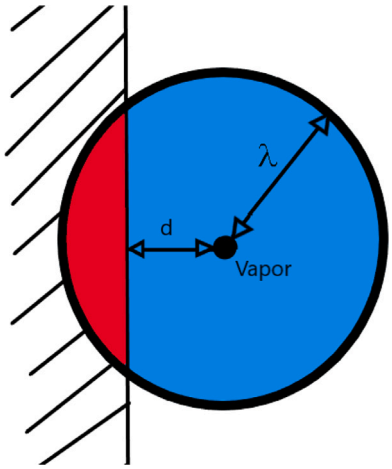

Fig. 14. d is the distance to the wall, λ is the mean free path of the vapour and the black dot represents the location of the vapour at time t. When the molecule is at the indicated location at time t, then it can be anywhere at the black circle at $t + \Delta t$. If the molecule reaches a location on the black circle that encloses the red area, then it has hit the wall. This is only possible when the vapour molecule is within a distance λ from the wall and the chance of hitting the wall decreases with increasing d.

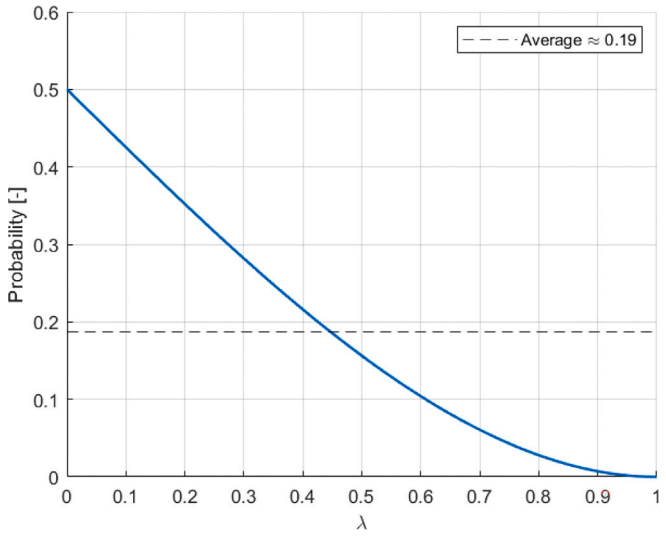

Fig. 15. Probability that a vapour particle hits the wall. Close to the wall the probability approaches 0.5 and at a distance $> \lambda$ the probability is zero.

radius of the particles, R' is the growth rate of the particles, A is the channel area and Θ_H represents the Heaviside function. This equation is used to determine the solid fraction along the whole channel.

A.4. Particle size distribution

The size of a particle r at the outlet of the channel, that nucleated at location z_0 with a size $R(z_0)$ can be written as follows, with R_∞ the size of the particle at the outlet of the channel:

$$r(z_0) = R_\infty - R(z_0) \tag{18}$$

From the conservation law, the concentration of such particles at the location of their origin $n(z_0)$ is determined:

$$\gamma_{\text{nuc}}(z_0)\ S(z_0)\ dz_0\ dt = n(z_0)\ u_{\text{gas}}(z_0)\ A(z_0)\ dt \tag{19}$$

This concentration depends significantly on the amount of particles nucleated in a partial volume of the channel. The left-hand side of Eq. (19) gives the number of particles nucleated in an infinitesimal volume $A(z_0)dz_0$ over an infinitesimal time interval dt. The right-hand side shows the same amount that is removed from this volume by the steady-state gas flow.

$$n(\infty, z_0)\ u_\infty\ A_\infty = n(z_0)\ u_{\text{gas}}(z_0)\ A(z_0) \tag{20}$$

Eq. (20) shows that the concentration of these particles at the outlet, $n(\infty, z_0)$, obeys the continuity equation. The equation relates the number of particles nucleated at z_0 that are present at the exit $n(\infty, z_0)$ to the concentration of particles nucleated at z_0 $n(z_0)$. In this equation, A_∞ is the cross-section near the outlet.

Knowing that $n(\infty, z_0)$ gives the concentration of particles of size $r(z_0)$, combining Eq. (19) and Eq. (20) and writing the equations as a function of r, by realising that $z_0(r)$ is the inverse of $r(z_0)$, the size distribution is obtained:

$$P(r)dr = \frac{\gamma_{\text{nuc}}\left(z_0(r)\right)}{u_\infty}\left|\frac{dr}{dz_0}\right|^{-1}\frac{A(z_0)}{A_\infty}dr \tag{21}$$

A.5. Wall interactions

In this section, the interactions of the flow with the icy walls are discussed. We consider accretion and sublimation, detailed in Appendix A.5.1 and Appendix A.5.2 respectively, and describe how these processes have been accounted for in the simulation of the crack's geometry evolution (Appendix A.5.3).

A.5.1. Accretion

Accretion on the walls of the vapour reduces the energy of the flow, since it carries internal and kinetic energy. Upon accretion to the walls, latent heat is produced due to phase change, and this heat is assumed to be conducted through the ice (Nakajima and Ingersoll, 2016). In the channel, the vapour travels at velocity V due to the flow, but also has a thermal velocity V_{th}:

$$V_{th} = \sqrt{\frac{8k_BT}{m\pi}} \tag{22}$$

In this expression, k_B is the Boltzmann constant and m is the mass of a H_2O molecule. This velocity follows random directions and causes the vapour particles to collide with the walls and with each other. The equation for the mean free path λ of the vapour is calculated as follows (Atkins and de Paula, 2007):

$$\lambda = V_{th}\Delta t = V_{th}/z = kT/\sigma \tag{23}$$

Δt is the time between collisions $[s]$, z is the collision frequency $[\text{s}^{-1}]$, k_B the Boltzmann constant, T the temperature [K], σ the cross-sectional area of a water molecule (assumed as $= (3A)^2 = 9 \cdot 10^{-20}$ m^2) and p the pressure $[pa]$. From this equation, Δt is derived to be:

$$\Delta t = k_BT/\sigma V_{th}p \tag{24}$$

The particles can only hit the walls within Δt when they are within a distance λ from the walls (see Fig. 14).

The probability of a particle hitting the wall within a distance λ, expressed as p_λ, can be computed. At a distance further than λ this probability is 0 and at a distance of close to zero from the wall the probability is 0.5. The probability within this distance is computed according to the ratio of the volume of the cap of the sphere that intersects the wall to the total volume of the sphere. h is the cap height, *i.e.* distance into the wall, $h = \lambda - d$, where d is the distance of the particle from the wall.

$$p_\lambda = \frac{V_{wall}}{V_{sphere}} = \frac{\pi h^2(\lambda - \frac{h}{3})}{\frac{4}{3}\pi\lambda^3} \tag{25}$$

The probability of a particle hitting the wall within Δt versus the distance to the wall is illustrated in Fig. 15, where the average probability $p_{\lambda,a} \approx 0.19$.

The average probability over the diameter of the channel is then determined as follows:

$$p_{channel} = p_\lambda\frac{2\lambda}{D} = p_\lambda\frac{\lambda}{r} \tag{26}$$

where $p_{channel}$ is the average probability of a particle hitting the wall from anywhere in the channel [-], D is the diameter of the channel and r is the radius of the channel. $p_{channel}$ must be multiplied with the sticking coefficient c_{stick} to determine the probability of a vapour particle sticking to the wall, this is called x.

$$x = p_{channel} \cdot c_{stick} = p_{\lambda} \frac{\lambda c_{stick}}{r} \tag{27}$$

x is then multiplied with total mass flow, resulting in the mass flux into the wall in a one-time step of Δt, *i.e.* the time in between collisions. The time that the flow is in one computational cell is:

$$t = \frac{dx}{V} \tag{28}$$

To determine the mass flow into the walls $\dot{m}_a$, this process is repeated $\frac{t}{\Delta t}$ times. The mass flow after Δt is then reduced to $(1-x)\cdot\dot{m}_{flow}$. Repeating this process results in:

$$\dot{m}_a = \sum_{i=1}^{n} x(1-x)^{n-1} \cdot \dot{m}_{flow} \tag{29}$$

The sticking coefficient of vapour on amorphous ice in the region of 220–273 K varies from 0.02–0.4 (Cuppen et al., 2010; Veeraghattam et al., 2014; Buch and Zhang, 1991). In our approach, we use the sticking coefficient provided in Buch and Zhang (1991):

$$c_{stick} = \left[\left(\frac{T}{102}\right) + 1\right]^{-2} \tag{30}$$

A.5.2. Sublimation

Sublimation of vapour from the walls is expected to increase the mass flow, indirectly affecting the momentum and energy of the flow. Since sublimation is an endothermic process, it could cool the flow. Sublimation is dominantly dependent on the wall temperature (Cuppen et al., 2010; Smith et al., 2016). The rate of sublimation R_{subl} [s^{-1}] is described as:

$$R_{subl} = \nu e^{\left(-\frac{E_b}{T_{ice}}\right)} \tag{31}$$

where ν is the pre-factor [s^{-1}], E_b is the binding energy [K] and T_{ice} is the ice temperature [K]. In our model, $\nu = 2.29 \cdot 10^{12}$ s^{-1} (Hasegawa et al., 1992) and $E = 5600$ K (Minissale et al., 2021).

The area occupied by one molecule H_2O on the wall is $(3Å)^2$, therefore the number of molecules per square meter is around 10^{19} $m^{-}2$. The rate of molecules sublimating per squared meter is, therefore, $R_{subl} \cdot 10^{19}$ [kg/m^2s]. This number is translated to the mass flow of sublimation $\dot{m}_s$ [kg/s] by using of the wall surface area S_w, the number of Avogadro $N_A = 6.022 \cdot 10^{23}$ mol^{-1} and the molar mass of water, M_{H_2O} (= 0.018 kg mol^{-1}), resulting in:

$$\dot{m}_s = S_w \frac{M_{H_2O}}{N_A} R_{subl} \cdot 10^{19} \tag{32}$$

The wall temperature gradient is set at 273 K near the reservoir and ∼ 230 K near the vent as a baseline (Nakajima and Ingersoll, 2016; Tenishev et al., 2014) and decreases linearly with the distance. For this reason, the sublimation is expected to be dominant in the lower regions of the channel.

A.5.3. Crack closing

Wall accretion and sublimation generate changes in channel geometry, as mentioned in Section 4.6. The total mass flux into the walls E is expressed in kg/m^2s and is generally positive, therefore accretion overpowers sublimation. The change from E to change in channel radius r is expressed as a function of E:

$$\frac{\partial r}{\partial t} = E \frac{N_A}{M_{H_2O}} V_{H_2O} \tag{33}$$

This conversion is done by changing the mass arriving on the walls [kg]/m^2 in the mass of the ice per m^2. Knowing that water molecules in ice are spaced bu 3 Å, there are $\sim 10^{19}$ molecules per m^2, which implies $10^{19} \cdot m_{H_2O}$ mass per m^2. One layer of water ice in thickness is also 3 Å(spacing between 2 water molecules). This allows us to convert the mass flux to an increase in thickness. In the equation, the constant values N_A, M_{H_2O} and V_{H_2O} are respectively the Avogadro number, the molar mass of water and the volume of a water molecule $\left(\frac{1}{3Å}\right)^3$.

References

Anderson, J.D., Wendt, J., 1995. Computational Fluid Dynamics, vol. 206, Springer.

Atkins, de Paula, 2007. Molecules in motion. Oxf. High. Educ. 272, 1–8.

Buch, V., Zhang, Q., 1991. Sticking probability of h and d atoms on amorphous ice-a computational study. Astrophys. J. 379, 647–652.

Burger, M., Sittler, Jr., E., Johnson, R., Smith, H., Tucker, O., Shematovich, V., 2007. Understanding the escape of water from enceladus. J. Geophys. Res. Space Phys. 112 (A6).

Čadek, O., Tobie, G., Van Hoolst, T., Massé, M., Choblet, G., Lefèvre, A., Mitri, G., Baland, R.M., Běhounková, M., Bourgeois, O., et al., 2016. Enceladus's internal ocean and ice shell constrained from cassini gravity, shape, and libration data. Geophys. Res. Lett. 43 (11), 5653–5660.

Cuppen, H., Kristensen, L., Gavardi, E., 2010. H2 reformation in post-shock regions. Mon. Not. R. Astron. Soc.: Lett. 406 (1), L11–L15.

Dong, Y., Hill, T., Teolis, B., Magee, B., Waite, J., 2011. The water vapor plumes of enceladus. J. Geophys. Res. Space Phys. 116 (A10).

Gao, P., Kopparla, P., Zhang, X., Ingersoll, A.P., 2016. Aggregate particles in the plumes of enceladus. Icarus 264, 227–238.

Hansen, C.J., Esposito, L., Stewart, A., Colwell, J., Hendrix, A., Pryor, W., Shemansky, D., West, R., 2006. Enceladus' water vapor plume. Science 311 (5766), 1422–1425.

Hansen, C., Esposito, L., Stewart, A., Meinke, B., Wallis, B., Colwell, J., Hendrix, A., Larsen, K., Pryor, W., Tian, F., 2008. Water vapour jets inside the plume of gas leaving enceladus. Nature 456 (7221), 477–479.

Hansen, C., Shemansky, D.E., Esposito, L.W., Stewart, A., Lewis, B., Colwell, J., Hendrix, A., West, R.A., Waite, Jr., J., Teolis, B., et al., 2011. The composition and structure of the enceladus plume. Geophys. Res. Lett. 38 (11).

Hasegawa, T.I., Herbst, E., Leung, C.M., 1992. Models of gas-grain chemistry in dense interstellar clouds with complex organic molecules. Astrophys. J. Suppl. Ser. 82, 167–195.

Hedman, M., Nicholson, P., Showalter, M., Brown, R., Buratti, B., Clark, R., 2009. Spectral observations of the Enceladus plume with Cassini-VIMS. Astrophys. J. 693 (2), 1749.

Ingersoll, A.P., Ewald, S.P., 2011. Total particulate mass in Enceladus plumes and mass of Saturn's E ring inferred from Cassini ISS images. Icarus 216 (2), 492–506.

Ingersoll, A.P., Ewald, S.P., Trumbo, S.K., 2020. Time variability of the Enceladus plumes: Orbital periods, decadal periods, and aperiodic change. Icarus 344, 113345.

Ingersoll, A.P., Nakajima, M., 2016. Controlled boiling on Enceladus. 2. Model of the liquid-filled cracks. Icarus 272, 319–326.

Jurac, S., Richardson, J., 2005. A self-consistent model of plasma and neutrals at saturn: Neutral cloud morphology. J. Geophys. Res. Space Phys. 110 (A9).

Khawaja, N., Postberg, F., Schmidt, J., 2017. The compositional profile of the enceladian ice plume from the latest cassini flybys. In: Lunar and Planetary Science Conference, Vol. 48.

Kieffer, S.W., Lu, X., Bethke, C.M., Spencer, J.R., Marshak, S., Navrotsky, A., 2006. A clathrate reservoir hypothesis for Enceladus' south polar plume. Science 314 (5806), 1764–1766.

Kieffer, S.W., Lu, X., McFarquhar, G., Wohletz, K.H., 2009. A redetermination of the ice/vapor ratio of Enceladus' plumes: Implications for sublimation and the lack of a liquid water reservoir. Icarus 203 (1), 238–241.

Lucchetti, A., Pozzobon, R., Mazzarini, F., Cremonese, G., Massironi, M., 2017. Brittle ice shell thickness of Enceladus from fracture distribution analysis. Icarus 297, 252–264.

Marti, J., Mauersberger, K., 1993. A survey and new measurements of ice vapor pressure at temperatures between 170 and 250K. Geophys. Res. Lett. 20 (5), 363–366.

Matson, D.L., Castillo-Rogez, J.C., Davies, A.G., Johnson, T.V., 2012. Enceladus: A hypothesis for bringing both heat and chemicals to the surface. Icarus 221 (1), 53–62.

Minissale, M., Aikawa, Y., Bergin, E., Bertin, M., Brown, W.A., Cazaux, S., Charnley, S., Coutens, A., Cuppen, H.M., 2021. Thermal desorption parameters of ices and their implications from snowlines to chemical complexity. J. Chem. Phys. 112 (70), 55.

Nakajima, M., Ingersoll, A.P., 2016. Controlled boiling on Enceladus. 1. Model of the vapor-driven jets. Icarus 272, 309–318.

Nimmo, F., Spencer, J., Pappalardo, R., Mullen, M., 2007. Shear heating as the origin of the plumes and heat flux on Enceladus. Nature 447 (7142), 289–291.

Peeters, P., Gielis, J., Van Dongen, M., 2002. The nucleation behavior of supercooled water vapor in helium. J. Chem. Phys. 117 (12), 5647–5653.

Porco, C., DiNino, D., Nimmo, F., 2014. How the geysers, tidal stresses, and thermal emission across the south polar terrain of Enceladus are related. Astron. J. 148 (3), 45.

Porco, C.C., Helfenstein, P., Thomas, P., Ingersoll, A., Wisdom, J., West, R., Neukum, G., Denk, T., Wagner, R., Roatsch, T., et al., 2006. Cassini observes the active south pole of Enceladus. Science 311 (5766), 1393–1401.

Postberg, F., Kempf, S., Rost, D., Stephan, T., Srama, R., Trieloff, M., Mocker, A., Goerlich, M., 2009a. Discriminating contamination from particle components in spectra of Cassini's dust detector CDA. Planet. Space Sci. 57 (12), 1359–1374.

Postberg, F., Kempf, S., Schmidt, J., Brilliantov, N., Beinsen, A., Abel, B., Buck, U., Srama, R., 2009b. Sodium salts in E-ring ice grains from an ocean below the surface of Enceladus. Nature 459 (7250), 1098–1101.

Saur, J., Schilling, N., Neubauer, F.M., Strobel, D.F., Simon, S., Dougherty, M.K., Russell, C.T., Pappalardo, R.T., 2008. Evidence for temporal variability of Enceladus' gas jets: Modeling of cassini observations. Geophys. Res. Lett. 35 (20).

Schmidt, J., Brilliantov, N., Spahn, F., Kempf, S., 2008. Slow dust in Enceladus' plume from condensation and wall collisions in tiger stripe fractures. Nature 451 (7179), 685–688.

Smith, H., Johnson, R., Perry, M., Mitchell, D., McNutt, R., Young, D., 2010. Enceladus plume variability and the neutral gas densities in Saturn's magnetosphere. J. Geophys. Res. Space Phys. 115 (A10).

Smith, R.S., May, R.A., Kay, B.D., 2016. Desorption kinetics of Ar, Kr, Xe, N2, O2, CO, methane, ethane, and propane from graphene and amorphous solid water surfaces. J. Phys. Chem. B 120 (8), 1979–1987.

Spencer, J.R., Barr, A.C., Esposito, L.W., Helfenstein, P., Ingersoll, A.P., Jaumann, R., McKay, C.P., Nimmo, F., Waite, J.H., 2009. Enceladus: An active cryovolcanic satellite. In: Saturn from Cassini-Huygens. pp. 73–199.

Spencer, J., Howett, C., Verbiscer, A., Hurford, T., Segura, M., Spencer, D., 2013. Enceladus heat flow from high spatial resolution thermal emission observations. EPSC Abstr. 8, 840–841.

Spencer, J., Nimmo, F., Ingersoll, A.P., Hurford, T., Kite, E., Rhoden, A., Schmidt, J., Howett, C., 2018. Plume origins and plumbing: from ocean to surface. Enceladus Icy Moons Saturn 163–174.

Tenishev, V., Öztürk, D.C.S., Combi, M.R., Rubin, M., Waite, J.H., Perry, M., 2014. Effect of the Tiger Stripes on the water vapor distribution in Enceladus' exosphere. J. Geophys. Res.: Planets 119 (12), 2658–2667.

Teolis, B.D., Perry, M.E., Hansen, C.J., Waite, J.H., Porco, C.C., Spencer, J.R., Howett, C.J., 2017. Enceladus plume structure and time variability: comparison of cassini observations. Astrobiology 17 (9), 926–940.

Tian, F., Stewart, A., Toon, O.B., Larsen, K.W., Esposito, L.W., 2007. Monte Carlo simulations of the water vapor plumes on Enceladus. Icarus 188 (1), 154–161.

Veeraghattam, V.K., Manrodt, K., Lewis, S.P., Stancil, P., 2014. The sticking of atomic hydrogen on amorphous water ice. Astrophys. J. 790 (1), 4.

Viisanen, Y., Strey, R., Reiss, H., 1993. Homogeneous nucleation rates for water. J. Chem. Phys. 99 (6), 4680–4692.

Wölk, J., Strey, R., 2001. Homogeneous nucleation of H2O and D2O in comparison: the isotope effect. J. Phys. Chem. B 105 (47), 11683–11701.

Wölk, J., Strey, R., Heath, C.H., Wyslouzil, B.E., 2002. Empirical function for homogeneous water nucleation rates. J. Chem. Phys. 117 (10), 4954–4960.

Zolotov, M.Y., 2007. An oceanic composition on early and today's Enceladus. Geophys. Res. Lett. 34 (23).